applied system innovation

MDPI

Article

Dynamic Investigation of a Solar-Driven Brayton Cycle with Supercritical CO_2

Christos Sammoutos, Angeliki Kitsopoulou, Panagiotis Lykas, Evangelos Bellos * and Christos Tzivanidis

Department of Thermal Engineering, School of Mechanical Engineering, National Technical University of Athens, 15780 Athens, Greece; chrissammoutos@hotmail.com (C.S.); akitsopoulou@mail.ntua.gr (A.K.); plykas@mail.ntua.gr (P.L.)
* Correspondence: bellose@central.ntua.gr

Abstract: The exploitation of solar irradiation is a critical weapon for facing the energy crisis and critical environmental problems. One of the most emerging solar technologies is the use of solar towers (or central receiver systems) coupled with high-performance thermodynamic cycles. In this direction, the present investigation examines a solar tower coupled to a closed-loop Brayton cycle which operates with supercritical CO_2 (sCO_2) as the working medium. The system also includes a storage system with two molten salt tanks for enabling proper thermal storage. The sCO_2 is an efficient fluid that presents significant advancements, mainly reduced compression work when it is compressed close to the critical point region. The novelty of the present work is based on the detailed dynamic investigation of the studied configuration for the year period using adjustable time step and its sizing for achieving a continuous operation, something that makes possible the establishment of this renewable technology as a reliable one. The analysis is conducted with a developed model in the Modelica programming language by also using the Dymola solver. According to the simulation results, the yearly solar thermal efficiency is 50.7%, the yearly thermodynamic cycle efficiency is 42.9% and the yearly total system efficiency is 18.0%.

Keywords: solar tower; Modelica; Brayton cycle; dynamic analysis; power production

check for updates

Citation: Sammoutos, C.; Kitsopoulou, A.; Lykas, P.; Bellos, E.; Tzivanidis, C. Dynamic Investigation of a Solar-Driven Brayton Cycle with Supercritical CO_2. *Appl. Syst. Innov.* **2023**, *6*, 71. https://doi.org/10.3390/asi6040071

Academic Editor: Sergio Nardini

Received: 5 July 2023
Revised: 29 July 2023
Accepted: 9 August 2023
Published: 10 August 2023

Copyright: © 2023 by the authors. Licensee MDPI, Basel, Switzerland. This article is an open access article distributed under the terms and conditions of the Creative Commons Attribution (CC BY) license (https://creativecommons.org/licenses/by/4.0/).

1. Introduction

The energy problem is one of the key issues facing humanity. The rapid development of technology in combination with the increase in world population has led to an increase in the demand for energy production [1,2]. In the previous decades, energy production was based on fossil fuels, a strategy that caused many environmental problems such as climate change, global warming and air pollution [3,4]. Since energy is a fundamental factor in humanity's growth, alternative energy sources are needed [5].

Renewable energy sources (RES) can perform a significant role in tackling the energy issue. Among all RES, solar energy is one of the most promising to encounter environmental and sustainability issues [6]. Solar energy is already being utilized for household needs [7]. However, solar energy is also a very promising source for power plants, especially concentrated solar power (CSP), with many CSP plants already operating or being under construction or investigation [8].

CSP plants' heat source is solar irradiance due to sunlight. Thus, this kind of power plant can be mostly found in areas with high direct normal irradiance (DNI) [9,10]. The concentrated irradiance is then converted to high thermal energy given to a heat transfer fluid (HTF). This energy can be utilized either directly or indirectly, where a CSP plant is integrated with a thermodynamic cycle for electricity production [11]. Among the CSP technologies, the most well-known and mature ones are the parabolic trough collector (PTC), the linear Fresnel reflector (LFR), the parabolic dish collector (PDC) and the solar

power tower (STP) [8]. The first two categories are considered linear focus applications, whereas the other two are considered point focus [9].

The most widely used technology is PTC, and the second is the STP technology [8]. These two are the most economically sustainable among the CSP categories [12]. Since STP is a single point focusing CSP, higher temperatures can be achieved in comparison to PTC [13]. STP technology can achieve temperatures greater than 1000 °C [14]. The main components of an STP are the heliostat field, the central receiver of the solar tower, the thermal energy storage (TES) and the power production configuration [13]. The heliostats reflect a percentage of DNI towards the central receiver. Thus, the temperature on the surface of the central receiver is increased, and, as a result, the temperature of the HTF is increased as well. Afterward, the HTF transfers its heat to a working fluid via a heat exchanger, which is used to produce power in a thermodynamic cycle [15,16]. For this application, as HTF, molten salt is preferred since it can operate at higher temperatures [17].

In the literature, there are many studies on CSP mainly focusing on the technology of the solar collector, the temperature, the HTF and the electricity production [10]. Some studies focus on calculating the DNI based on the geometry of the solar field. Gauché et al. [9] have used solar angle calculations, whereas He et al. [18] have used the ray tracing process of sunlight. A new method for designing the heliostat field proposed by Wei et al. [19] saves time on the design and optimization process of the field. The annual mean optical efficiency was improved by 0.09%. Many studies focus on the calculations of central's receiver heat losses. For example, Kim et al. [20] have presented a numerical simulation using computational fluid dynamics (CFD) to calculate the total thermal losses for the central receiver, and the proposed model predicted the convection and total heat losses of the central receiver with an average absolute deviation of 11.4% and 5.9%, respectively. In addition, Jadhav et al. [21] have proposed a mathematical model based on algebraic equations. Furthermore, Hasuike et al. [22] have proposed a numerical simulation for the prediction of the characteristics of the central receiver. The radiation-to-heat conversion efficiency for the proposed design of the central receiver was found to be 90%. Additionally, some other studies focused on the calculations for the HTF. Albarbar et al. [23] have presented a methodology for calculating the thermal losses of the HTF.

Furthermore, in the literature, there are a lot of studies presenting calculations for the overall layout of an STP. Awan et al. [14] have used the particle swarm optimization technique to design and optimize an STP. Although the solar-to-electricity efficiency was found to be decreased by 0.9%, the annual energy output of the STP was increased by approximately 160 GWh. Zhang et al. [24] have developed a mathematical model with the lumped parameter method to verify the dynamic characteristics of an existing STP. Additionally, Sorgulu et al. [25] have proposed an STP for both electricity and freshwater production based on reverse osmosis technology, with a total flow rate of 240.02 kg/s of water being obtained. Moreover, Yang et al. [26] have suggested a hybrid STP, decreasing the heat losses of the central receiver due to convection and radiation by 24.8% and 42.4%, respectively. Finally, Habibi et al. [15] have proposed the combination of a central receiver system with both a Brayton and an organic Rankine cycle (ORC), where if the CO_2 is chosen as the working fluid for the Brayton cycle, the total exergy efficiency increases while the cycle pressure ratio also increases.

In the current study, a detailed dynamic investigation of a solar-driven Brayton cycle operating with supercritical carbon dioxide (sCO_2) is presented. The solar thermal system is a central receiver system using two thermal storages. The simulation has been conducted using the Dymola software, where all the parts of the proposed configuration were programmed using the Modelica programming language in the Dymola environment. The simulation with this tool presents the possibility for an analysis with a high level of detail using an adjustable time step, as well as the application of advanced control techniques. Specifically, this study proposes a simple but accurate modeling based on analytical equations for calculating the performance of an STP, taking advantage of the Modelica language to solve the algebraic equation system without the need to provide a specific computational

strategy. Different components have been developed, and they have been inserted in the Dymola environment by using the proper connections among them. The parameters of the problem have to do with the solar thermal system and the thermodynamic cycle, as well as with the followed control strategy.

2. Material and Methods

2.1. The Studied Configuration

The studied configuration consists of a solar thermal system, which is a central receiver system. The heliostats have a two-axis tracking system to follow the sun's orbit during the day [27]. The central receiver is in the form of a solar tower with a cylindrical geometry for the receiver. Additionally, the solar thermal system has two thermal storages, and the chosen HTF is molten salt. Finally, two pumps are used to ensure the flow of the HTF [15].

The thermodynamic system is integrated with the solar thermal system using a countercurrent heat exchanger. The thermodynamic cycle is chosen to be a Brayton cycle because it shows good behavior in transient operation [28]. In addition, a recuperator is used to increase thermal efficiency [29]. The working fluid is chosen to be sCO_2 because of its thermodynamic properties and characteristics [28,29]. Figure 1 depicts the studied configuration, an STP with a central receiver system integrated with a supercritical Brayton cycle (SCBC).

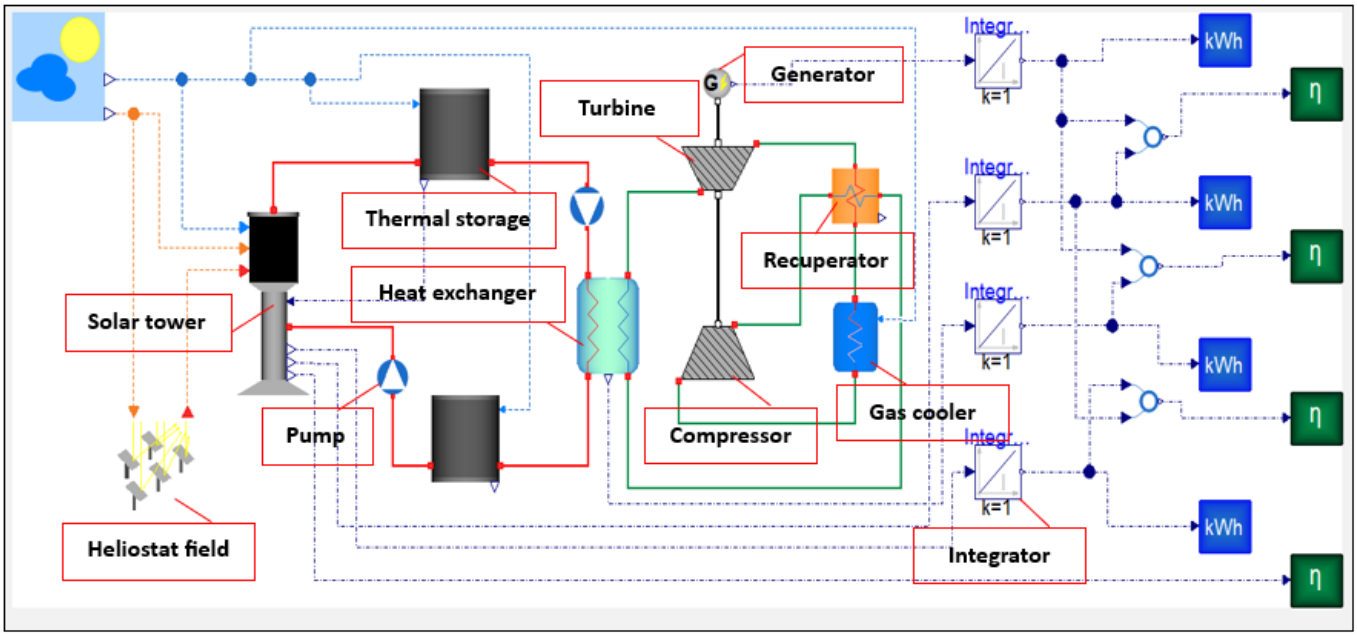


Figure 1. System configuration of a solar-driven Brayton cycle.

2.2. Modeling of the Solar Tower

The modeling of the solar field is based on the basic energy balances of a CSP. The solar field consists of the heliostats and the solar tower, which is responsible for raising the temperature of the HTF. The optical efficiency (η_o) of the solar field can be calculated using the equation below [27]:

$$\eta_o = \eta_{mir} \times \eta_{atm} \times \eta_{spill} \times \eta_{cos} \times \eta_{S\&B} \quad (1)$$

The mirror efficiency (η_{mir}) represents the heliostat's efficiency of reflectivity which strongly depends on the material and the quality of the surface of a heliostat [27]. The atmospheric efficiency (η_{atm}) represents the losses of irradiance which, although reflected by the heliostats, does not reach the central receiver of the solar tower but is either absorbed or scattered into the atmosphere [27]. The spillage efficiency (η_{spill}) represents the losses

incurred due to various system errors, such as the orientation of the heliostats to monitor the sun's orbit. The last two efficiencies depend on the distance between the heliostat and the central receiver. As this distance increases, these efficiencies decrease. Moreover, as the total area of the heliostat increases, the spillage efficiency decreases [27]. The cosine efficiency (η_{cos}) depends on the relative position between the sun, the heliostat and the central receiver. For the north hemisphere, heliostats placed on the north side of the solar tower have a higher cosine efficiency [27]. Finally, the shading and blocking efficiency ($\eta_{S\&B}$) represents the losses due to the arrangement of the heliostat field [27].

The total available solar irradiance (Q_{sol}) is the total available heat input for the solar field and can be calculated using the equation below, where A_{mir} represents the total area of the heliostats and DNI is the direct normal irradiance [14,15].

$$Q_{sol} = A_{mir} \times DNI \tag{2}$$

The total heat absorbed by the central receiver (Q_{abs}) can be calculated with the below equation using the total optical efficiency of the solar field [13].

$$Q_{abs} = \eta_o \times Q_{sol} \tag{3}$$

Additionally, the total heat absorbed can be calculated as the sum of the useful heat (Q_u) and thermal losses (Q_{loss}), as shown in the equation below [13].

$$Q_{abs} = Q_u + Q_{loss} \tag{4}$$

The useful heat (Q_u) can be calculated using the heat transfer from the central receiver to the HTF using the equation below. The overall heat transfer coefficient of the heat exchanger (U_{ex}) represents the total heat transfer between the surface of the central receiver and its internal heat exchanger where the HTF flows. Additionally, the total area of this heat exchanger (A_{ex}) needs to be known. The useful heat gained by the HTF is calculated based on the temperature difference between the central receiver's surface temperature (T_r) and the mean fluid temperature (T_{fm}) [30].

$$Q_u = U_{ex} \times A_{ex} \times (T_r - T_{fm}) \tag{5}$$

The mean fluid temperature (T_{fm}) can be calculated as the mean of the inlet (T_{in}) and the outlet (T_{out}) temperature of the HTF flowing through the internal heat exchanger of the central receiver, as shown in the equation below [23].

$$T_{fm} = \frac{T_{s,out} + T_{s,in}}{2} \tag{6}$$

Additionally, the useful heat can be calculated based on the energy balance in the fluid volume, using the equation below, where ($\dot{m}_s$) is the molten salt's mass flow rate. The average specific heat of the molten salt ($C_{p,s,avg}$) at constant pressure is calculated based on its average temperature [15].

$$Q_u = \dot{m}_s \times C_{p,s,avg} \times (T_{s,out} - T_{s,in}) \tag{7}$$

The thermal losses from the surface of the central receiver to the ambient (Q_{loss}) are the sum of the radiation (Q_{rad}) and convection (Q_{conv}) losses, and they can be calculated using the equation below. Any contact losses between the central receiver and the body of the tower are neglected [15].

$$Q_{loss} = Q_{conv} + Q_{rad} \tag{8}$$

The thermal losses due to convection (Q_{conv}) can be calculated using the equation below, where the area of the central receiver (A_r) is the collateral surface of the cylinder,

h_{out} is the heat transfer coefficient due to convection between the central receiver and the ambient and T_{amb} is the ambient temperature [13].

$$Q_{conv} = A_r \times h_{out} \times (T_r - T_{amb}) \quad (9)$$

The radiation thermal losses (Q_{rad}) can be calculated using the equation below, where ε_r is the emissivity of the outer surface of the central receiver and σ is the Stefan–Boltzmann constant [23].

$$Q_{rad} = A_r \times \varepsilon_r \times \sigma \times \left({T_r}^4 - {T_{amb}}^4\right) \quad (10)$$

The heat transfer coefficient due to convection between the central receiver and the ambient (h_{out}) can be calculated based on the average Nusselt number using the equation below, where k_{air} is the thermal conductivity of air and D_r is the diameter of the cylindrical surface of the central receiver [30].

$$h_{out} = \frac{Nu \times k_{air}}{D_r} \quad (11)$$

The average Nusselt number for a cross flow on a circular cylinder (Nu_D) can be calculated according to the following equation (Churchill and Bernstein), considering that the product between Reynolds and Prandtl number is greater than 0.2 [30].

$$Nu_D = 0.3 + \frac{0.62 \times {Re_D}^{1/2} \times Pr^{1/3}}{\left[1 + \left(\frac{0.4}{Pr}\right)^{2/3}\right]^{1/4}} \times \left[1 + \left(\frac{Re_D}{282,000}\right)^{\frac{5}{8}}\right]^{4/5} \quad (12)$$

The Reynold number for a cross flow on the outer surface of a circular cylinder (Re_D) can be calculated based on the following equation [30].

$$Re_D = \frac{u_{air} \times D_r}{\nu_{air}} \quad (13)$$

The Prandtl number (Pr) for air can be calculated using the following equation [31].

$$Pr = \frac{\mu_{air} \times C_{p,air}}{k_{air}} \quad (14)$$

2.3. Modeling of the Storage Tanks

Thermal energy (TES) storage tanks are essential for STPs. Solar thermal power plants can store thermal energy, in contrast to other RES that can only store electrical energy [32]. Using a thermal storage tank allows for the readjustment of power production according to electricity consumption peak hours rather than solar irradiance peak hours [33]. In STPs, two thermal storage tanks are used, one for the hot stream of the HTF and one for the cold stream, right after the outlet of the heat exchanger between the solar thermal system and the thermodynamic cycle. The HTF is charged through the central receiver due to the absorbed solar heat, stored in the tank and then discharged to feed the coupled thermodynamic cycle through the heat exchanger [34].

For STPs, the HTF chosen is molten salt because of the higher temperature rate in which it can be used, in comparison with other HTF_s such as water and thermal oils [17]. Molten salt is a chemical compound that under normal conditions has the structure of a solid salt, but at high temperatures it liquefies [35]. The three main thermodynamic properties of interest are the melting point (T_m), the density (ρ_s) and the heat capacity under constant pressure of the molten salt ($C_{p,s}$). The density of the molten salt (ρ_s) is

calculated using the equation below, where R_s is the initial density at 0 °C and B_s is the density variation according to temperature [35].

$$\rho_s = R_s - B_s \times (T_s - 273.15) \quad (15)$$

The TES is modeled based on mass and energy balance. The mass balance equation is shown below. The stored mass flow rate ($\dot{m}_{st}$) is the difference between the inlet ($\dot{m}_{in}$) and outlet ($\dot{m}_{out}$) mass flow rate of the molten salt [32].

$$\dot{m}_{st} = \dot{m}_{in} - \dot{m}_{out} \quad (16)$$

The stored heat (Q_{st}) is calculated using the energy balance equation for the thermal storage tank, given by the following equilibrium [26].

$$Q_{st} = Q_{in} - Q_{loss} - Q_{out} \quad (17)$$

The storage heat input (Q_{in}) is calculated using the equation below, where the inlet temperature of the salt ($T_{s,in}$) is taken to be the outlet temperature from the central receiver, where $\dot{m}_{s,in}$ is the mass flow rate that enters the TES [26].

$$Q_{in} = \dot{m}_{s,in} \times C_{p,s,avg} \times (T_{s,in} - T_{amb}) \quad (18)$$

The storage heat output (Q_{out}) is calculated with the following equation, where $\dot{m}_{s,out}$ is the mass flow rate that exits the TES [26].

$$Q_{out} = \dot{m}_{s,out} \times C_{p,s,avg} \times (T_{s,st} - T_{amb}) \quad (19)$$

The thermal losses from the storage surface to the ambient are calculated using the equation below. The overall heat transfer coefficient of the tank (U_t) depends on the structural materials of the tank's shell and needs to be as low as possible to reduce thermal losses to the ambient. The area of the storage used to calculate the total thermal losses (A_t) is the sum of the collateral surface of the cylindrical-shaped storage and the surface on top of it, which is considered a circle [32].

$$Q_{loss} = U_t \times A_t \times (T_{st} - T_{amb}) \quad (20)$$

Finally, the temperature of the stored molten salt (T_{st}) is calculated using the equation below, where the volume (V_s) is considered to be the instantaneous volume of the molten salt and ρ_s the instantaneous density of it [14,26].

$$Q_{st} = \rho_s \times C_{p,s,avg} \times V_s \times \frac{dT_{st}}{dt} \quad (21)$$

Pumps are used to secure the mass flow rate of the molten salt in the solar thermal cycle. The pump work (W_{pump}) can be calculated using the equation below, where $h_{s,out}$, and $h_{s,in}$ are the specific enthalpies of the molten salt at the outlet and the inlet of the pump, respectively [26].

$$W_{pump} = \dot{m}_s \times (h_{s,out} - h_{s,in}) \quad (22)$$

2.4. Modeling of the Brayton Cycle

The thermodynamic cycle is modeled as a regenerative Brayton cycle (RBC), where the working fluid is set to be the sCO_2. This fluid's level of safety is the highest possible [36]. The main advantage of CO_2 is the low critical temperature, allowing even low-temperature sources to be exploited [36]. Furthermore, the use of supercritical fluid enables an avoidance of the complexity of the phase-changing process that occurs for every working fluid [28,36]. Working with low pressure near the critical pressure of the fluid implies high C_p values. Additionally, in high temperatures, the thermodynamic properties of CO_2 are identified

with the ideal gas properties [28]. Finally, the size of the turbomachinery can be significantly reduced compared to a steam turbine in a conventional ORC [29].

The heat input in this cycle is provided by a heat exchanger, which is the component of the total system that connects the solar thermal system with the thermodynamic cycle. This heat exchanger is modeled using the number of transfer units method (NTU). The heat of the hot stream ($Q_{hot,s}$), i.e., the molten salt, is calculated by using the following equation [37].

$$Q_{hot,s} = \dot{m}_s \times C_{p,s,avg} \times (T_{s,in} - T_{s,out}) \quad (23)$$

The heat of the cold stream ($Q_{cold,CO2}$), i.e., CO_2, is calculated using the equation below. These two heat values, the $Q_{hot,s}$ and the $Q_{cold,CO2}$, must be equal [37].

$$Q_{cold,CO_2} = \dot{m}_{CO_2} \times C_{p,CO_2} \times (T_{CO_2,out} - T_{CO_2,in}) \quad (24)$$

The effectiveness of the heat exchanger (ε) is calculated using the following equation, where the heat exchanger is chosen to be counter-current [37].

$$\varepsilon = \frac{1 - \exp\left(-\left(1 - \frac{CF_{min}}{CF_{max}}\right) \times \frac{U_{ex} \times A_{ex}}{CF_{min}}\right)}{1 - \frac{CF_{min}}{CF_{max}} \times \exp\left(-\left(1 - \frac{CF_{min}}{CF_{max}}\right) \times \frac{U_{ex} \times A_{ex}}{CF_{min}}\right)} \quad (25)$$

The equation below calculates the product (CF) of the mass flow rate ($\dot{m}_f$) with the mean heat capacity (C_f) of the fluid. This product is calculated for both streams of the heat exchanger. In the current study, these two streams are the molten salt stream and the CO_2 stream. Its maximum (CF_{max}) or minimum (CF_{min}) value refers to the comparison between these product values for the molten salt and CO_2 as fluids [37].

$$CF = \dot{m}_f \times C_f \quad (26)$$

The outlet temperature of the hot stream ($T_{s,out}$) is finally calculated using the equation below, where $\dot{m}_s$ is the mass flow rate of the molten salt [37].

$$\varepsilon = \frac{\dot{m}_s \times C_{p,s,avg} \times (T_{s,in} - T_{s,out})}{CF_{min} \times (T_{s,in} - T_{CO_2,in})} \quad (27)$$

The total power output of the turbine (P_{turb}) is calculated based on the following equation, where $\eta_{m,turb}$ is the mechanical efficiency of the turbine, $\dot{m}_{CO_2}$ is the mass flow rate of the carbon dioxide and $h_{in,turb}$ and $h_{out,turb}$ are the specific enthalpies of the carbon dioxide at the inlet and the outlet of the turbine, respectively [30]:

$$P_{turb} = \eta_{m,turb} \times \dot{m}_{CO_2} \times (h_{in,turb} - h_{out,turb}) \quad (28)$$

The thermodynamic properties of CO_2 are used according to the table of properties of the fluid [38]. Because all the thermodynamic properties of CO_2 in the inlet of the turbine are known, the entropy is also known. Due to this, the isentropic enthalpy of the expansion ($h'_{out,turb}$) can be found, and then, using the following equation which represents the definition of the turbine's isentropic efficiency ($\eta_{is,turb}$), the real enthalpy at the outlet ($h_{out,turb}$) of the turbine can then be calculated [39].

$$\eta_{is,turb} = \frac{h_{in,turb} - h_{out,turb}}{h_{in,turb} - h\prime_{out,turb}} \quad (29)$$

The total power consumed by the compressor (P_{comp}) is calculated by the following equation, where $\eta_{m,comp}$ is the mechanical efficiency of the turbine, $\dot{m}_{CO_2}$ is the mass flow

rate of the carbon dioxide and $h_{in,comp}$ and $h_{out,comp}$ are the specific enthalpies of the carbon dioxide at the inlet and the outlet of the turbine, respectively [30].

$$P_{comp} = \dot{m}_{CO_2} \times \left(h_{out,comp} - h_{in,comp}\right) / \eta_{m,comp} \quad (30)$$

The enthalpy at the outlet of the compressor ($h_{out,comp}$) is calculated using the equation below, which refers to the isentropic efficiency of the compressor [39].

$$\eta_{is,comp} = \frac{h\prime_{out,comp} - h_{in,comp}}{h_{out,comp} - h_{in,comp}} \quad (31)$$

This power is supplied to the compressor from the turbine through the common shaft that connects the turbomachinery of the cycle. Thus, the net power output (P_{net}) is calculated by subtracting the consumed power of the compressor (P_{comp}) from the total power output of the turbine (P_{turb}), using the equation below [39].

$$P_{net} = P_{turb} - P_{comp} \quad (32)$$

Additionally, in this model a recuperator is used, aiming to increase the total cycle efficiency. This recuperator is modeled based on the NTU method for a counter-current heat exchanger [37]. Moreover, this part of the cycle is modeled so that, if the temperature of CO_2 at the outlet of the compressor is greater than the temperature at the outlet of the turbine, the recuperator is being bypassed [40].

The gas cooler in the cycle cools the working fluid before it enters the compressor. The temperature at the inlet of the compressor is chosen to be 5K greater than the ambient temperature [41]. The cooling fluid is chosen to be air since these kinds of power plants are installed in areas where water cannot be wasted [27]. The gas cooler is also modeled based on the NTU method. The C_p used for the CO_2 is the one for the inlet of the working fluid in the gas cooler [39].

Finally, the net electrical power output of the system (P_{el}) is calculated based on the mechanical ($\eta_{m,g}$) and electrical losses (η_{el}) of the generator, using the equation below [40].

$$P_{el} = P_{net} \times \eta_{m,g} \times \eta_{el} \quad (33)$$

2.5. Evaluation Indexes

The indexes that evaluate the current model are the characteristic efficiency values of the power plant. The yearly amount of energy (E) is calculated as the integral of the time fluctuation of power or heat flux. The equation below shows the integral for the calculation of annual energy [27].

$$E_i = \int_0^t Q_i dt \quad (34)$$

The yearly thermal efficiency (η_{th}) is calculated using the equation below, where E_u is the useful energy produced by the central receiver and E_{sol} is the total available energy of the solar field.

$$\eta_{th} = \frac{E_u}{E_{sol}} \quad (35)$$

The yearly thermodynamic efficiency of the Brayton cycle (η_{cycle}) is calculated using the equation below, where E_{net} is the net energy produced by the thermodynamic cycle and E_{in} is the input in the cycle, calculated as the integral of hot streams ($Q_{hot,s}$) of the system's heat exchanger [39].

$$\eta_{cycle} = \frac{E_{net}}{E_{in}} \quad (36)$$

Finally, the yearly total system efficiency (η_{sys}) is calculated with the following equation [14].

$$\eta_{sys} = \frac{E_{net}}{E_{sol}} \quad (37)$$

2.6. Simulation Strategy

In the present study, the solar-driven Brayton cycle system is modeled using the Dymola software. Each component of the total system is modeled based on the Modelica programming language. The present model of the system, which is depicted in Figure 1, models the simulation of the STP for a year. Each model is created based on certain parameters, which are different for each one. The parameters needed to define each component are presented in the following tables. Then, the interfaces between the models are created to establish cooperation between the models. Interfaces are called connectors in the Dymola software. These connectors are specific model types for the Modelica programming language. These cannot be simulated, but they contain variables that, two components connected, need to transfer from one to the other. For each component, the needed type of connector is selected. For example, the solar tower model interacts with the heliostat field model to receive the value of the total available solar irradiance (Q_{sol}).

For the heliostat model, the heliostat "Sanlúcar 120" is chosen [42]. The distance between two consecutive heliostats is chosen to be 1 m, while the distance between the first heliostat and the solar tower is set to be 30 m. The input in this model is the DNI, where the output is the available solar irradiance of the field (Q_{sol}). Table 1 shows the heliostat field parameters.

Table 1. Heliostat field parameters [42].

Parameters	Values/Description
Heliostat	Sanlúcar 120
Count	700
Length	12.84 m
Width	9.45 m
Reflectivity (η_{mir})	0.88

For the solar tower model, both parameters for the central receiver and the molten salt need to be provided. This model requires three inputs. Firstly, Q_{sol} from the heliostat model is needed to calculate the total absorbed heat (Q_{abs}) by the central receiver. In addition, the ambient temperature has to be known in order to calculate the thermal losses. Finally, the DNI is used as a control parameter to avoid negative values for the useful heat (Q_u). These negative values may appear since, although there is no heat input in the central receiver during the night, there are still thermal losses because of the high temperature of the central receiver's surface [14]. The material of the central receiver is chosen to be aluminum [43], while the overall coefficient of heat transfer for the central receiver's inner surface is set to be 22 W/m^2K [22]. The emissivity is doubled in order to approach the real radiation losses for high temperatures. Table 2 shows the parameters of the solar tower. The individual efficiencies of the solar field are also shown in Table 2.

The molten salt chosen for this simulation is "$NaNO_3$ (18%)-KNO_3 (53%)-$LiNO_3$ (29%)". The composition is presented in percentage by weight (wt%). This molten salt has a lower melting point and higher specific heat capacity in comparison to the most used salt, "KNO_3 (40%)-$NaNO_3$ (60%)", also known as "solar salt". The mass flow rate of the molten salt in the solar thermal system is chosen so that the maximum temperature of the molten salt does not exist as the maximum limit of stability [17]. Moreover, when the temperature of the stored molten salt is less than a certain temperature level, the mass flow of the molten

salt in the heat exchanger of the STP is reduced to 0.1 kg/s to allow the thermal storage to charge. Table 3 shows the parameters of the molten salt.

Table 2. Design parameters for the receiver.

Solar Tower's Geometry [14]	
Tower's height	190 m
Receiver's shape	Cylindrical
Receiver's height	18.2 m
Receiver's diameter	15.2 m
Central Receiver's Material [22,43]	
Material	Aluminum 1100-H12
Emissivity	0.1
Internal Heat Exchanger [22]	
$U_{r,ex}$	22 W/m^2K
$A_{r,ex}$	40,000 m^2
Solar Field Efficiencies [42]	
η_{atm}	0.95
η_{spill}	0.99
η_{cos}	0.83
$\eta_{S\&B}$	0.93

Table 3. Thermophysical properties of molten salt [17].

Parameters	**Values/Description**
Molten salt	$NaNO_3$ (18%)-KNO_3 (53%)-$LiNO_3$ (29%)
Maximum temperature	540 °C
Melting point	120 °C
Specific heat capacity	1640 J/kgK

Finally, the thermophysical properties of the air are needed to calculate the heat transfer coefficient between the central receiver and the ambient. The wind speed is set to be constant at 10 m/s, where the parameters that affect the Prandtl number of the air are functions of the ambient temperature [31]. For simplicity, the thermophysical properties of the air are set to be constant, considering the properties at 30 °C. Table 4 shows the thermophysical properties of air.

Table 4. Thermophysical properties of air at 30 °C [31].

Properties	**Values**
k_{air}	0.026 W/mK
v_{air}	13×10^{-6} m^2/s
μ_{air}	17×10^{-6} kg/ms
$C_{p,air}$	1100 J/kgK

For the thermal storage system, two tanks are needed for the STP [14]. Using the Dymola software allows for the creation of only one model for thermal storage. By duplicating the model and setting different parameters for each copy of the model, two different tanks

can be modeled based on the same thermal storage model. For this model, the ambient temperature needs to be an input in order to calculate the total thermal losses from the tank to the ambient. The storage surface consists of three layers [44]. The first material is chosen to be carbon steel [45], the second layer is an insulation layer of firebricks [46], and finally, the last layer is stainless steel [47]. Table 5 shows the materials chosen for the storage's surface, leading to an overall heat transfer coefficient of 1.5 W/m^2K.

Table 5. Materials of TES.

Materials [44]	**Thermal Conductivity**
ASTM A516 Carbon Steel 70 Grade	52 W/mK
Firebrick	0.099 W/mK
Flexible AISI 321H stainless steel	15 W/mK (at 20 °C)

The initial conditions of the simulation are the total molten salt's stored mass and temperature in the two thermal storages. The stored volume of the molten salt (V_s) must be less than the total volume of the storage. This value depends on the mass flow rate at the inlet and the outlet of the storage but also on the temperature of the stored molten salt, since this variable affects its density. Table 6 shows the density parameters of the chosen molten salt [35], as well as the initial conditions for the simulation. Table 6 shows the geometry parameters of the TES_s.

Table 6. Design parameters of TES.

Density Parameters	
R_s	2083 kg/m^3
B_s	0.715 kg/m^3K
Initial Conditions	
Mass stored	8,000,000 kg
Temperature stored	500 K
Geometry	
Number of storage tanks	2
Shape	Cylindrical
Height	10 m
Diameter	30 m

The heat exchanger is modeled based on the NTU method [37]. Its type is chosen to be counter-current. The parameters of the heat exchanger are chosen to achieve high effectiveness. Additionally, the recuperator's model, as well as the gas cooler's parameters, are chosen to achieve high effectiveness. Table 7 presents the parameters for all the heat exchangers of the total system model.

The turbomachinery modeling consists of three separate models: the turbine model, the compressor model and the generator model. All three machines are connected to the same shaft. The mass flow rate of the CO_2 is constant. The pressure ratio value must be between two and three to achieve the highest efficiency [28]. Additionally, the low pressure of the Brayton cycle is chosen to be higher than the critical pressure of CO_2 to secure the supercritical conditions of the working fluid. At the same time, the low pressure of the cycle has to be close to the critical pressure, because the specific heat capacity at constant pressure presents a maximum value at the critical point [28]. The isentropic efficiency of the turbine is higher than the compressor's isentropic efficiency [48]. Table 8 presents

the design parameters of the turbomachinery. The pressure ratio of both the turbine and compressor are the same since the pressure losses of the heat exchanger are neglected.

Table 7. Design parameters of the heat exchanger.

Main Heat Exchanger	
U_{ex}	50 W/m^2K
A_{ex}	3000 m^2
Recuperator	
U_{reg}	50 W/m^2K
A_{reg}	2500 m^2
Gas Cooler	
U_{gc}	40 W/m^2K
A_{gc}	900 m^2
$\dot{m}_{gc}$	150 kg/s
$C_{p,air}$	1000 J/kgK

Table 8. Design parameters of the turbomachinery.

Turbine	
$\eta_{is,T}$	0.93
$\eta_{m,T}$	0.98
$\dot{m}_{CO_2}$	55 kg/s
p_{max}	200 bar
p_{min}	75 bar
Pressure ratio	2.67
Compressor	
$\eta_{is,C}$	0.89
$\eta_{m,C}$	0.98
Generator	
$\eta_{m,g}$	0.98
$\eta_{el,g}$	0.99

The weather model provides two inputs into the STP system, the ambient temperature and the DNI. These values are extracted from the PVGIS database [49]. Because the data is given in hourly variation and the dynamic simulation is based on seconds, interpolation is needed to adjust the input data on the dynamic solver. The data used in the current study are for Athens, Greece. The starting time for the simulation process is set to 0, where the stopping time is set to 8760 h. The chosen integration algorithm is "Dassl", and the interval length is chosen to be 3600 s.

3. Results and Discussion

3.1. Weather Data of the Examined Location

The simulation is being processed for one simulation year. The two input variables into the modeled system are the ambient temperature and the DNI [49]. The chosen location is Athens, Greece. Figure 2 shows the annual ambient temperature variation. Figure 3 shows the annual DNI variation [49].

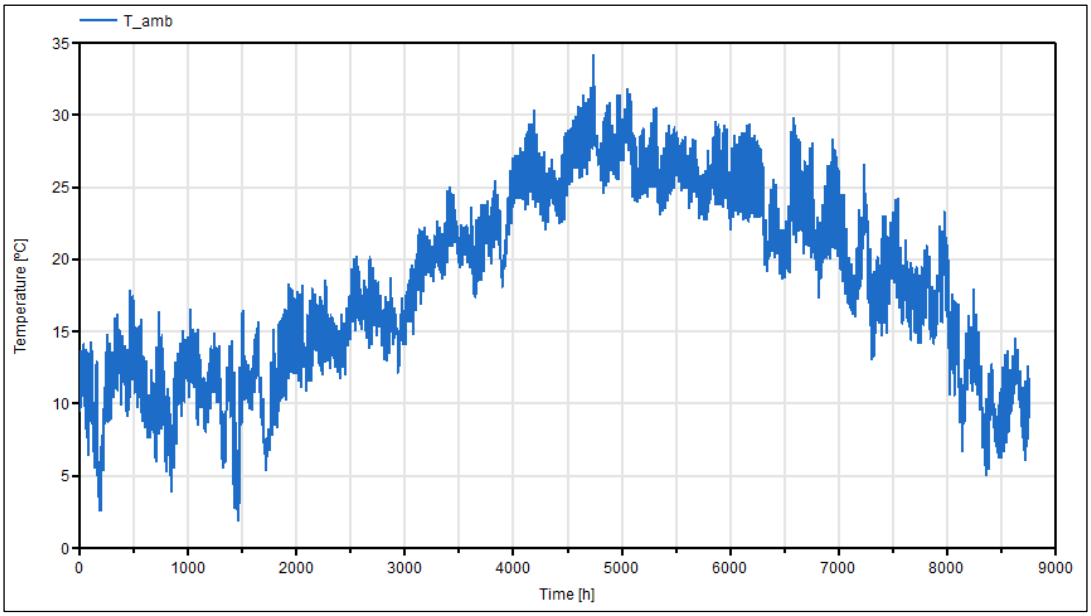


Figure 2. Annual ambient temperature variation for Athens, Greece.

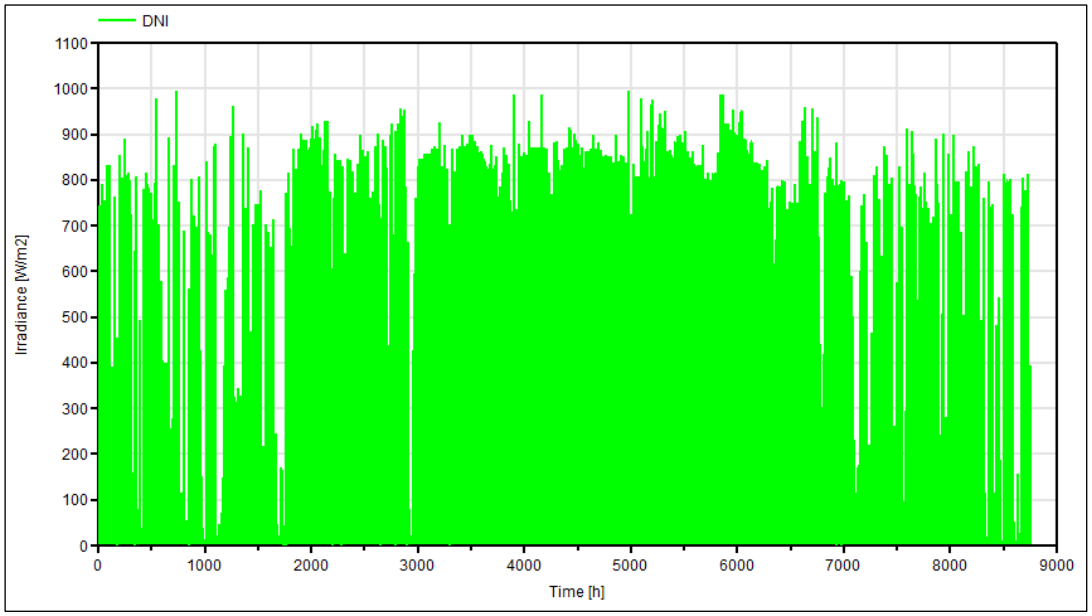


Figure 3. Annual DNI's variation for Athens.

3.2. Central Receiver's Results

Figure 4 shows the yearly temperature variation of the central receiver's surface. This temperature seems to increase when the DNI density increases. This density increases throughout the summer months. The maximum temperature of the central receiver's surface appears to be 541.6 °C on the 26th of July. The melting point of the chosen material for the central receiver's surface is 643 °C [43].

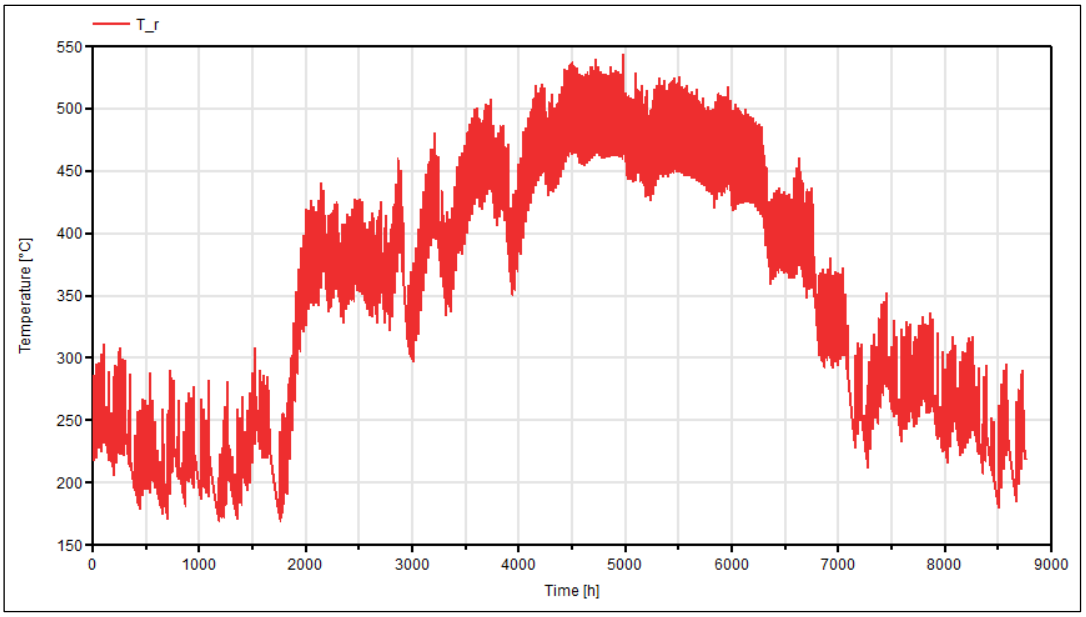


Figure 4. Annual central receiver's outer surface temperature.

Figure 5 shows the heat fluxes of the solar thermal system. The maximum heat flux of the system must be the Q_{sol}. The Q_u is zero for several consecutive operational hours throughout the year. This result is due to the control system applied to avoid negative values of Q_u during the simulation. The higher the Q_u value, the higher the instant solar thermal efficiency. The maximum Q_{sol} is on the 1st of February, with a value of 73.3 MW_{th}, but the maximum density of Q_{sol} appears during the summer months. The maximum Q_u is found to be 47.5 MW_{th} on the same day. As a result, the maximum daily solar thermal efficiency is found to be 64.8%.

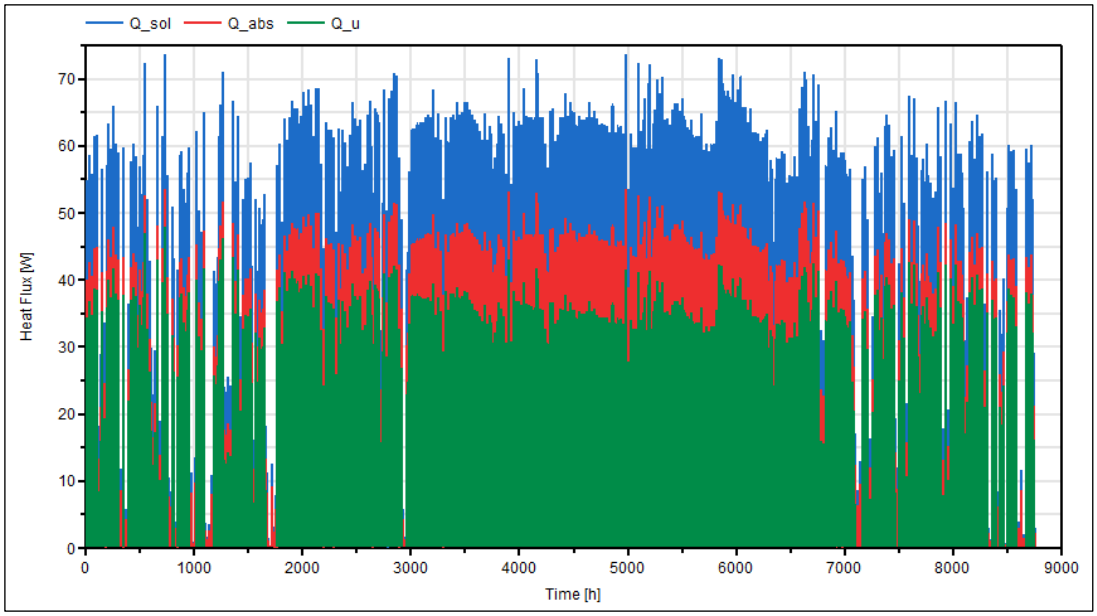


Figure 5. Annual heat fluxes of total solar irradiance (Q_{sol}), total heat absorbed (Q_{abs}) and useful heat (Q_u) for the solar thermal system.

Figure 6 depicts the total thermal losses in comparison to the absorbed heat by the central receiver. The total thermal losses are never equal to zero, not even through the night,

although the solar irradiance is zero. The reason for this is that, although the Q_{sol} is zero, the central receiver still has a higher surface temperature than the ambient. As a result, there are thermal losses due to convection with the ambient and radiation throughout the year. The maximum total thermal losses are during the summer months. This is because, although the ambient temperature rises, the temperature on the central receiver's surface rises at a higher rate, leading to an increase in total thermal losses.

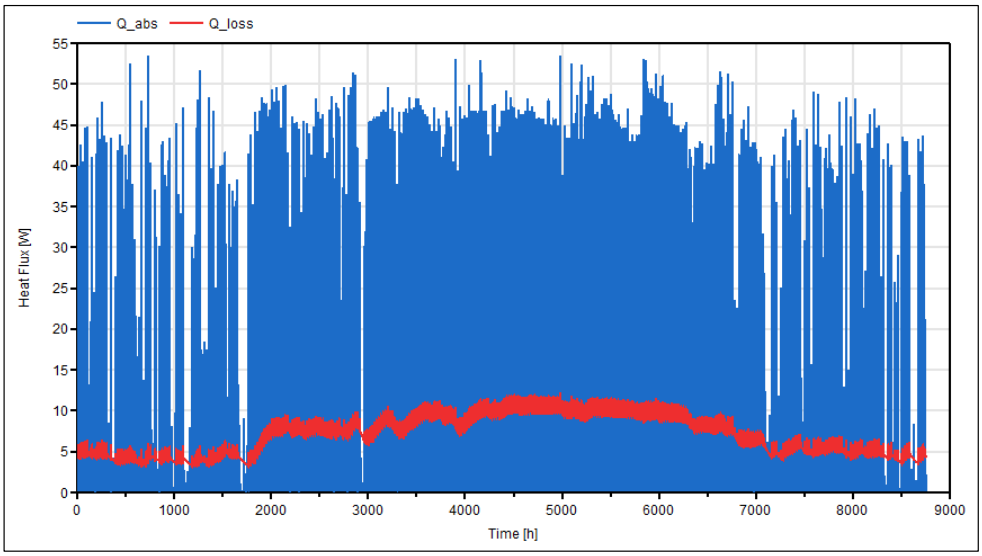


Figure 6. Annual total thermal losses (Q_{loss}) of the solar thermal system in comparison with the total absorbed heat (Q_{abs}).

The total thermal losses are the sum of thermal losses due to convection with the ambient air and radiation. Figure 7 depicts the two parameters of thermal losses. Thermal losses due to convection are higher than those due to radiation. During the summer months, the percentage the total thermal losses that are convection losses has a maximum value of 83%, and the corresponding percentage of the radiation losses is 17%.

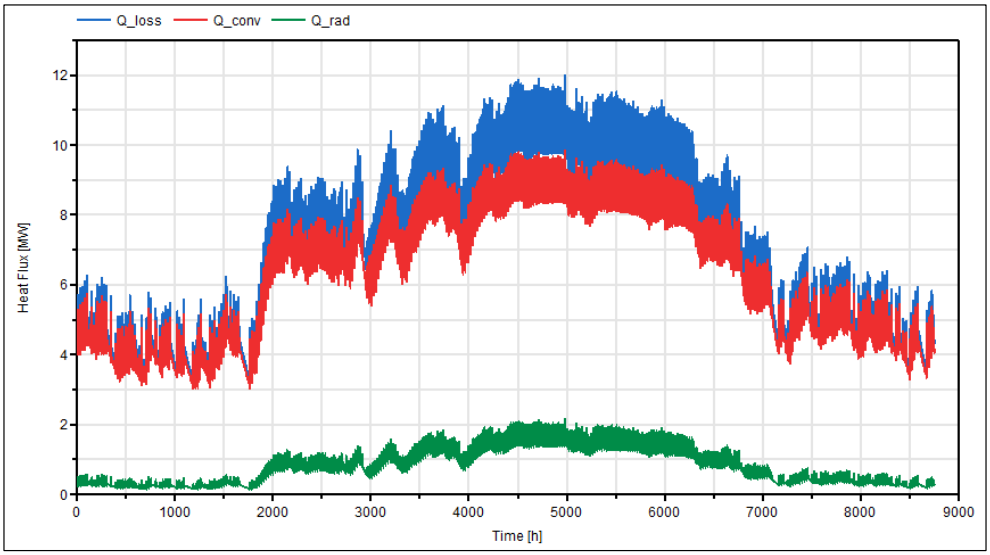


Figure 7. Annual total thermal losses (Q_{loss}), thermal losses due to convection (Q_{conv}) and thermal losses due to radiation (Q_{rad}) for the solar thermal system.

Figure 8 depicts the temperature variation of the molten salt stored in the high-temperature TES. This temperature must be within the temperature boundaries of the chosen molten salt. The lower limit is the melting point, while the upper limit is the maximum temperature at which the molten salt maintains stability. The maximum temperature of the molten salt is 507.9 °C, whereas the minimum temperature found in the cold TES, located before the solar tower, is 170.4 °C. The volume capacity of the hot TES reaches 65.9%, and the minimum density is found to be 1.72 g/cm^3. Figure 9 depicts the level of the volume capacity for the hot TES. This level expresses the ratio of the molten salt's volume to the tank's volume.

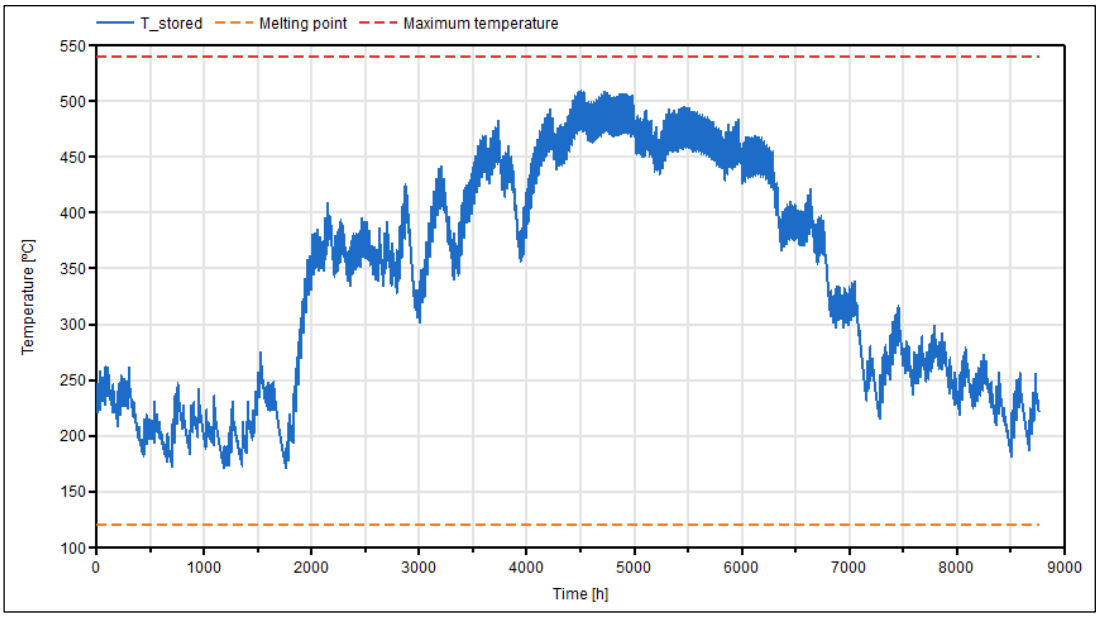


Figure 8. Annual temperature variation of molten salt (T_{st}) in the hot TES.

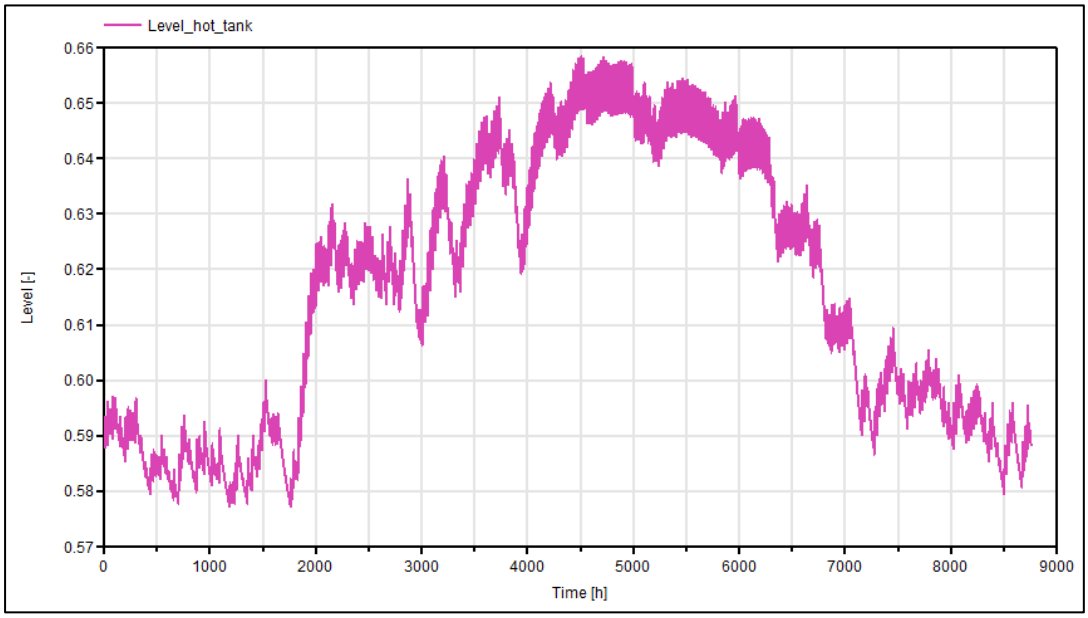


Figure 9. Annual variation in the ratio of molten salt's volume to tank's volume for the hot TES.

3.3. Heat Exchanger's Results

The system has three heat exchangers. Firstly, there is the heat exchanger that integrates the solar thermal system with the thermodynamic cycle. The thermodynamic cycle has one recuperator and a gas cooler. Figure 10 shows the temperature variation of the two streams flowing in the main heat exchanger of the system. The outlet temperature of the CO_2 appears to be slightly lower than the inlet temperature of the hot molten salt. The yearly average effectiveness of the heat exchanger is 0.92. The maximum inlet temperature of the thermodynamic cycle is 488.2 °C.

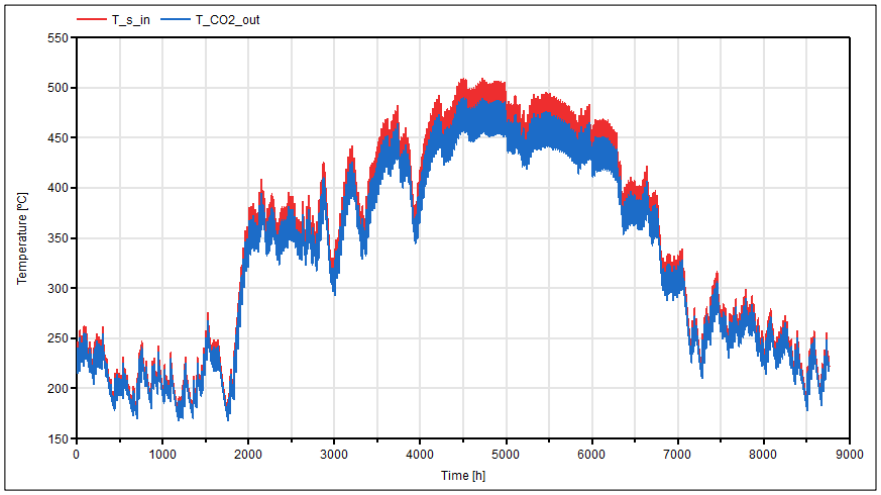


Figure 10. Annual temperature variation for the inlet stream of molten salt ($T_{s,in}$) and the outlet stream of CO_2 ($T_{CO2,out}$) for the heat exchanger between the solar thermal system and the thermodynamic cycle.

Figure 11 depicts the temperature variation for the two streams entering the recuperator of the thermodynamic cycle. The recuperator raises the temperature of the CO_2 stream before it enters the heat exchanger of the system. By using the regeneration method effectively, the total efficiency of the thermodynamic cycle increases, and as a result the total efficiency of the system also increases. The maximum increase achieved is 150.8 °C. The average effectiveness of the recuperator is 0.73. Figure 12 depicts the temperature variation in the gas cooler. The cooling air exists in the gas cooler at a maximum temperature of 83.3 °C.

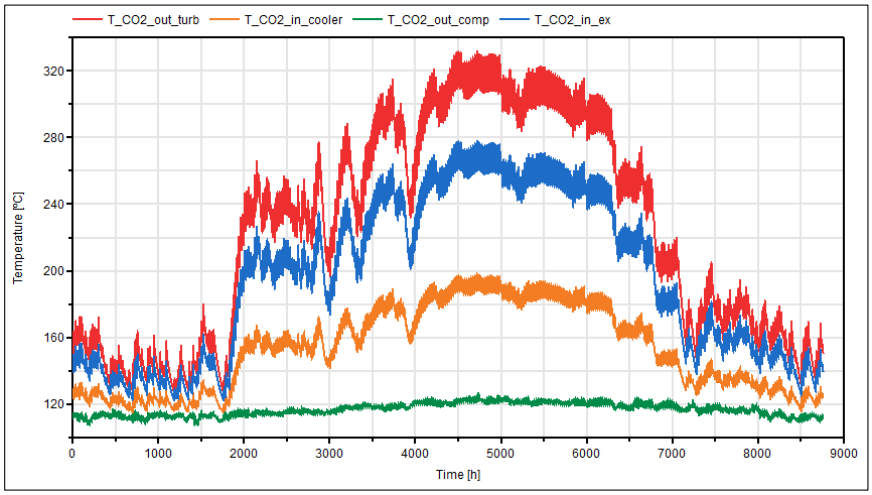


Figure 11. Temperature variation of both CO_2 streams flowing through the recuperator of the thermodynamic cycle.

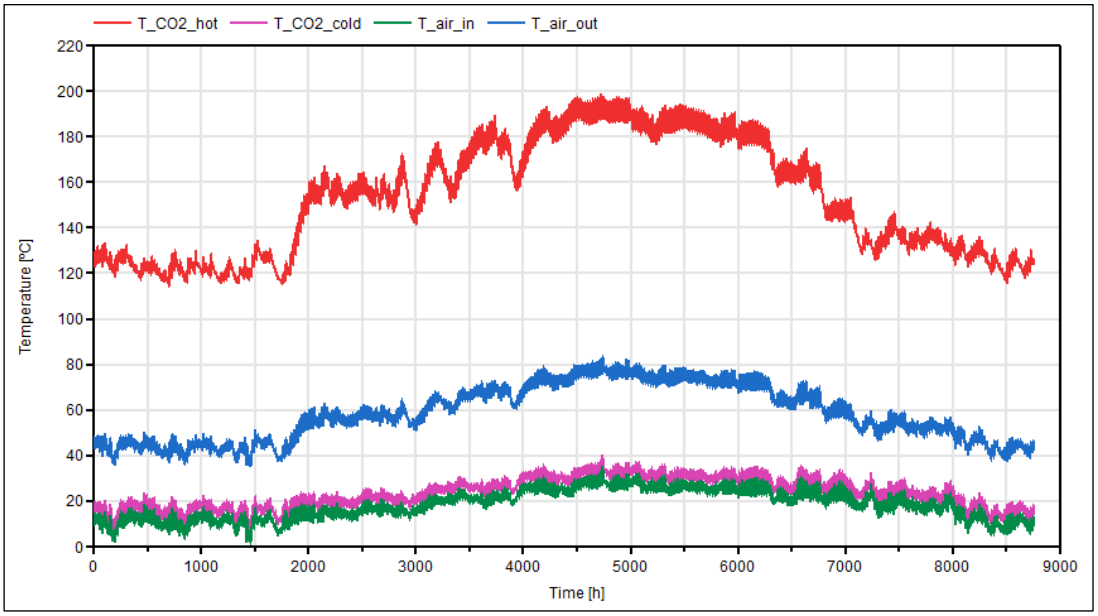


Figure 12. Temperature variation of CO_2 and air stream flowing through the gas cooler of the thermodynamic cycle.

3.4. Thermodynamic Cycle's Results

The net power output of the thermodynamic cycle is depicted in Figure 13. This power output must be less than the total heat input in the thermodynamic cycle, which is the total heat flux of the heat exchanger. As can be seen, the thermodynamic efficiency of the cycle decreases during the summer months. The maximum heat input into the cycle is 12.1 MW_{th}, where the net power output for the same simulation time is found to be 4.08 MW_{th}, leading to a minimum thermal efficiency of the cycle equal to 33.7%.

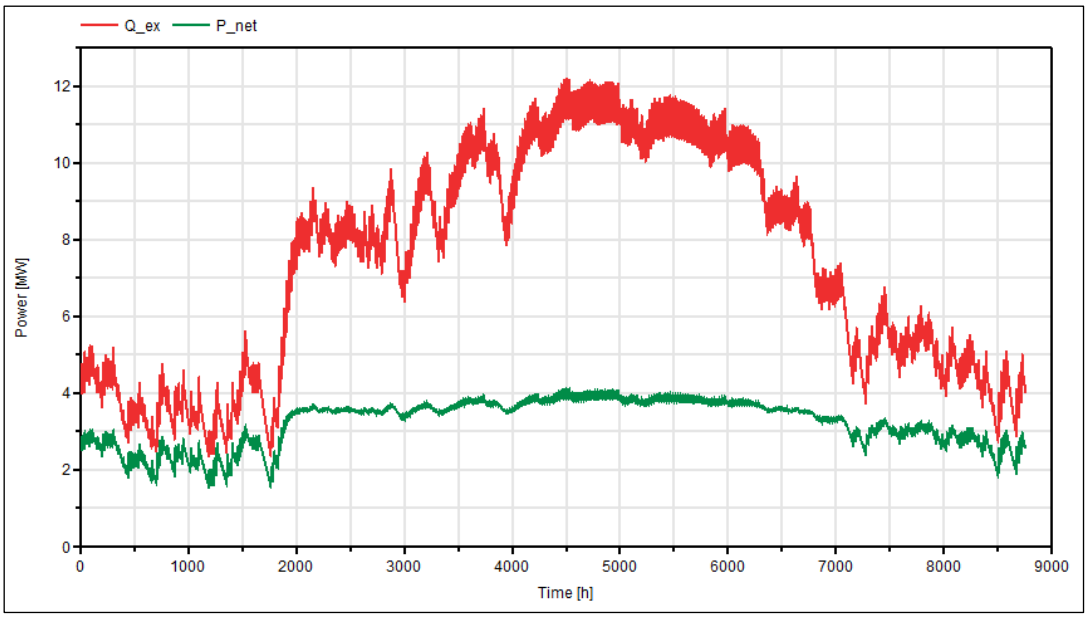


Figure 13. Net power output (P_{net}) and total heat input (Q_{ex}) of the thermodynamic cycle.

Figure 14 depicts the inlet and outlet temperature of the gas turbine. The maximum temperature of the turbine is 488.2 °C, which is less than the temperature limit of a turbine

for a sCO_2 Brayton cycle, which, with the current technology, is estimated to be a maximum of 1500 °C [40].

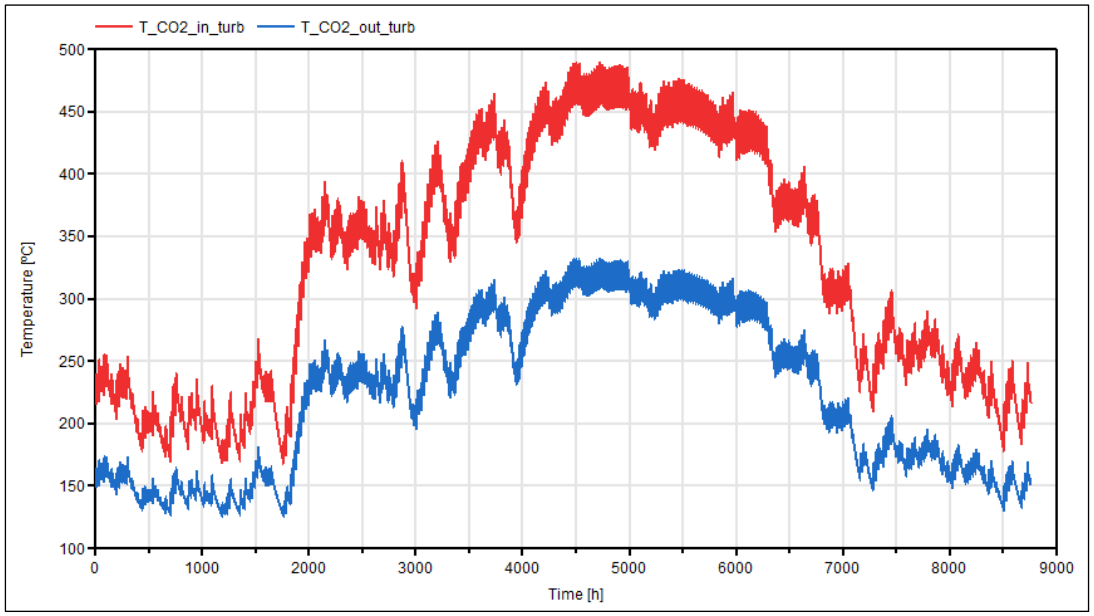


Figure 14. Annual inlet and outlet temperature of the gas turbine.

Figure 15 depicts the annual net electrical power output of the STP. This value is never equal to zero. This happens because of the use of thermal storage, which allows the STP to operate during the nighttime when solar irradiance is not available. The maximum value of P_{el} is found to be 4.01 MW_{el}, and the minimum is found to be 1.56 MW_{el}.

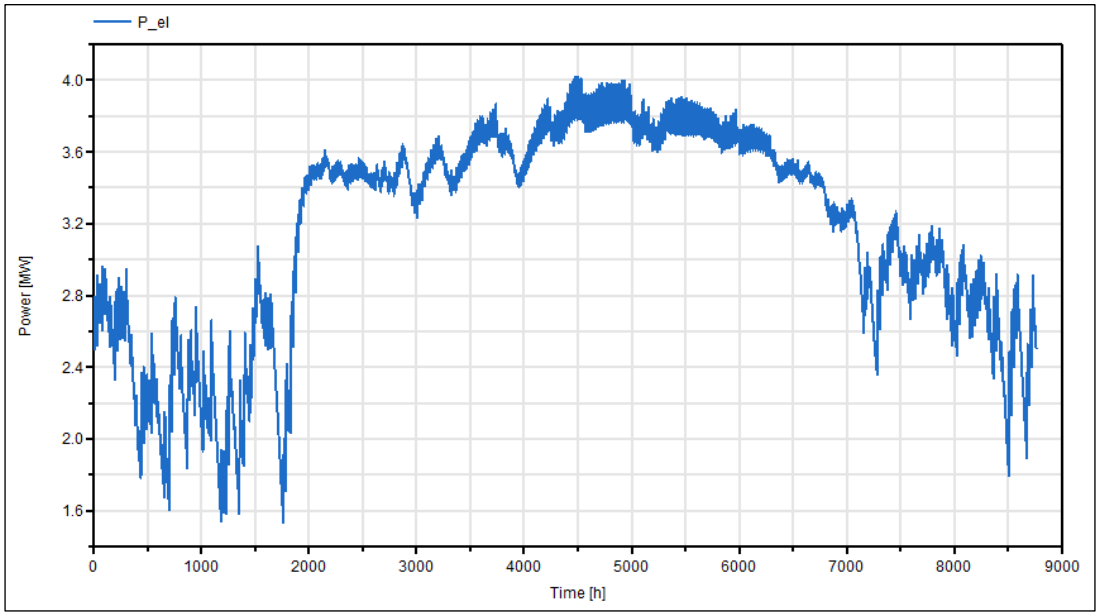


Figure 15. Annual net electrical power output (P_{el}) of the STP.

3.5. Daily Analysis

Figure 16 depicts the daily variation in the solar thermal and the total system efficiencies for a chosen day of the year, the 25th of March. It can be observed that, during the first hours in the morning, as well as the last hours before sunset, the system efficiency is

increasing. This happens although the thermal efficiency decreases. The reason for this is the existence of the TES system, which allows the STP to keep operating. The total system efficiency is shown to be zero since is the multiplication of the solar thermal efficiency with the thermodynamic efficiency and the total system losses, although the thermodynamic efficiency is not zero and net power output is still produced. Figure 17 depicts the daily variation in these two efficiencies for another day of the year, the 25th of August, where the total efficiency of the system exists even if the solar thermal efficiency is zero.

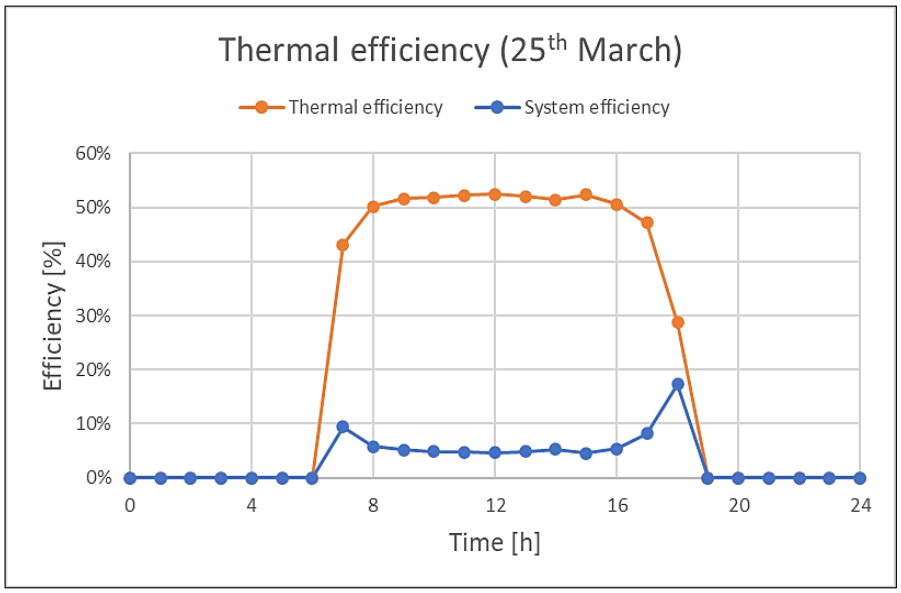


Figure 16. Daily variation in thermal efficiency (η_{th}) and system efficiency (η_{sys}) for the 25th of March.

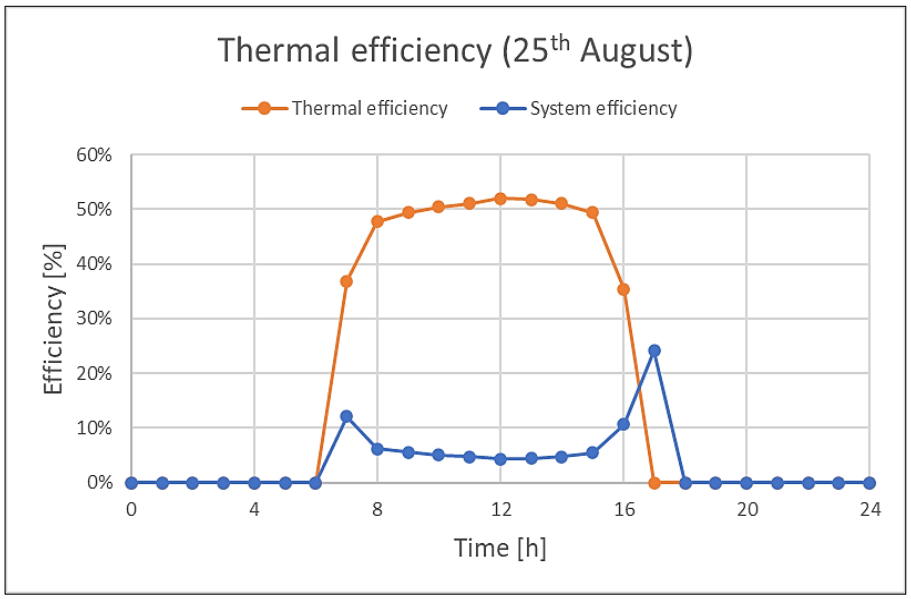


Figure 17. Daily variation in thermal efficiency (η_{th}) and system efficiency (η_{sys}) for the 25th of August.

3.6. Yearly Performance and Discussion

The yearly performance of the STP can be expressed using four efficiency indexes. The first efficiency index is the optical efficiency of the solar field. The second important efficiency index is the thermal solar, and the third is the efficiency of the thermodynamic cycle. The last and most important index of the system is the total efficiency of the STP. Table 9 shows the annual average efficiencies of the STP. It also provides values for these

indexes from the literature, allowing the comparison between these values. The reported results of the present work are close to the reported results of the literature. Thus, the conclusions of the present work are reasonable, and the developed model can be accepted as a reliable one.

Table 9. Annual average efficiency indexes for STP modeling.

	Efficiency Index [%]			
Studies	η_o	η_{th}	η_{cycle}	η_{sys}
Current study	63.8	50.7	42.9	18.0
Habibi et al. [15]	65.0	-	35.4	-
Wei et al. [19]	64.1	-	-	-
He et al. [18]	67.1	-	-	-
Awan et al. [14]	-	-	-	16.7

Moreover, it is useful to add that the incorporation of the recuperator enhances the system and the thermodynamic cycle efficiencies. Specifically, the operation without the recuperator leads to 16.1% system efficiency, while the use of a recuperator leads to 18% presenting and an increase of about 11.8%. Moreover, the use of the recuperator enhances the thermodynamic efficiency from 34.2% to 42.9%.

4. Conclusions

In this study, a dynamic investigation of a solar-driven power plant was conducted. This STP integrates a solar thermal system with a Brayton cycle through a counter-current heat exchanger. The solar thermal system is a solar tower, combined with a heliostat field and two TES. The Brayton cycle operates with sCO_2 as its working fluid. The modeling of the solar thermal system was created based on the mass and energy balance analysis. The modeling of the thermodynamic cycle was created based on the fundamentals of thermodynamics. The mathematical modeling for all the components that form the total system was developed using Modelica, a powerful programming language for modeling dynamic systems. The simulation process was done using the Dymola software, a software that integrates and simulates models based on Modelica.

The main conclusions of this study are the following:

- The optical efficiency was found to be 63.8%, whereas the thermal efficiency was found to be 50.7%. The thermodynamic efficiency of the cycle was calculated at 42.9%, and finally, the total system efficiency was 18.0%.
- The total thermal losses of the central receiver are mainly the result of the thermal losses due to convection, but thermal losses due to radiation also exist.
- The total system efficiency presents an increasing rate during the first hours of sunlight and the last hours before sunset. This efficiency increase is due to the usage of the two TES.
- The net electrical power output presents a peak during the summer, where the density of DNI is higher and the TES is fully charged.
- The use of a recuperator increases the system and the thermodynamic cycle efficiencies. Without the use of such a regenerator, the annual average system efficiency is found to be 16.1%, and the annual average thermodynamic cycle efficiency is found to be 34.2%. These values are significantly lower compared to the respective values of 18% for the system efficiency and 42.9% for the cycle efficiency with the recuperator.

In the future, the present system will be optimized, and it will also be examined for different climate conditions. Moreover, different configurations of gas turbines can be examined, for example, with intercooling in the compression and multi-stage expansion with reheating. Furthermore, economic and environmental analysis can be performed.

Author Contributions: Conceptualization, C.S., E.B., C.T.; methodology, C.S., A.K., P.L., E.B.; software, C.S., A.K., E.B.; investigation, C.S., A.K., E.B.; resources, C.S., P.L.; data curation, C.S., A.K., P.L.; writing—original draft preparation, C.S., A.K., P.L., E.B., C.T.; writing—review and editing, C.S., A.K., P.L., E.B., C.T.; supervision, E.B., C.T. All authors have read and agreed to the published version of the manuscript.

Funding: This research received no external funding.

Institutional Review Board Statement: Not applicable.

Informed Consent Statement: Not applicable.

Data Availability Statement: Available after request.

Conflicts of Interest: The authors declare no conflict of interest.

Nomenclature

Symbol	Description	Units
A	Area	m^2
B	Density variation	kg/m^3K
C	Specific heat capacity	J/kgK
CF	Product of mass flow rate with specific heat	W/K
Cp	Specific heat capacity at constant pressure	J/kgK
D	Diameter	m
E	Energy	kWh
h	Specific enthalpy	J/kg
h′	Isentropic specific enthalpy	J/kg
hout	Heat transfer coefficient between receiver and the ambient	W/m^2K
k	Thermal conductivity	W/mK
$\dot{m}$	Mass flow	kg/s
Nu	Nusselt number	-
P	Power	W
p	Pressure	bar
Pr	Prandtl number	-
Q	Heat flux	W
R	Initial density at 0 °C	kg/m^3
Re	Reynolds number	-
T	Temperature	K
U	Overall heat transfer coefficient	W/m^2K
u	Velocity	m/s
V	Volume	m^3
v	Kinematic viscosity	m^2/s
W	Work	W

Greek symbols

ε	Emissivity	-
η	Efficiency	-
μ	Dynamic viscosity	kg/ms
σ	Stefan-Boltzmann constant (=5.67×10^{-8})	W/m^2K^4

Subscripts

abs	absorbed
air	air
amb	ambient
atm	atmospheric
avg	average
comp	compressor
co2	carbon dioxide
cold	cold
conv	convection

cos	cosine
cycle	thermodynamic cycle
d	diameter
el	electrical
ex	exchanger
f	fluid
fm	mean fluid
g	generator
gc	gas cooler
hot	hot
in	inlet
is	isentropic
loss	losses
m	mechanical
max	maximum
min	minimum
mir	mirror
net	net
o	optical
out	outlet
p	pressure
r	receiver
rad	radiation
reg	recuperator or regenerator
S&B	shading and blocking
s	molten salt
sol	solar
spill	spillage
st	stored
sys	system
turb	turbine
t	tank
th	solar thermal
u	useful
wt	by weight percentage

Abbreviations

CFD	Computational Fluid Dynamics
CSP	Concentrated Solar Power
DNI	Direct Normal Irradiance
HTF	Heat Transfer Fluid
LFR	Linear Fresnel Reflector
NTU	Number of Transfer Units
ORC	Organic Rankine Cycle
PDC	Parabolic Dish Collector
RBC	Regenerative Brayton Cycle
SCBC	Supercritical Brayton Cycle
STP	Solar Tower Plant
sCO_2	Supercritical Carbon Dioxide
TES	Thermal Energy Storage

References

1. Behzadi, A.; Arabkoohsar, A. Feasibility study of a smart building energy system comprising solar PV/T panels and a heat storage unit. *Energy* **2020**, *210*, 118528. [CrossRef]
2. Tyagi, V.V.; Rahim, N.A.A.; Rahim, N.A.; Jeyraj, A. Progress in solar PV technology: Research and achievement. *Renew. Sustain. Energy Rev.* **2013**, *20*, 443–461. [CrossRef]

3. Alirahmi, S.M.; Mousavi, S.F.; Ahmadi, P.; Arabkoohsar, A. Soft computing analysis of a compressed air energy storage and SOFC system via different artificial neural network architecture and tri-objective grey wolf optimization. *Energy* **2021**, *236*, 121412. [CrossRef]
4. Sampaio, P.G.V.; González, M.O.A. Photovoltaic solar energy: Conceptual framework. *Renew. Sustain. Energy Rev.* **2017**, *74*, 590–601. [CrossRef]
5. Bhattacharya, T.; Chakraborty, A.K.; Pal, K. Effects of Ambient Temperature and Wind Speed on Performance of Monocrystalline Solar Photovoltaic Module in Tripura, India. *J. Sol. Energy* **2014**, *2014*, 817078. [CrossRef]
6. Qazi, A.; Hussain, F.; Rahim, N.A.; Hardaker, G.; Alghazzawi, D.; Shaban, K.; Haruna, K. Towards Sustainable Energy: A Systematic Review of Renewable Energy Sources, Technologies, and Public Opinions. *IEEE Access* **2019**, *7*, 63837–63851. [CrossRef]
7. Behzadi, A.; Arabkoohsar, A.; Yang, Y. Optimization and dynamic techno-economic analysis of a novel PVT-based smart building energy system. *Appl. Therm. Eng.* **2020**, *181*, 115926. [CrossRef]
8. Achkari, O.; El Fadar, A. Latest developments on TES and CSP technologies—Energy and environmental issues, applications and research trends. *Appl. Therm. Eng.* **2020**, *167*, 114806. [CrossRef]
9. Gauché, P.; Rudman, J.; Mabaso, M.; Landman, W.A.; von Backström, T.W.; Brent, A.C. System value and progress of CSP. *Sol. Energy* **2017**, *152*, 106–139. [CrossRef]
10. Islam, M.T.; Huda, N.; Abdullah, A.B.; Saidur, R. A comprehensive review of state-of-the-art concentrating solar power (CSP) technologies: Current status and research trends. *Renew. Sustain. Energy Rev.* **2018**, *91*, 987–1018. [CrossRef]
11. Fernández, A.G.; Gomez-Vidal, J.; Oró, E.; Kruizenga, A.; Solé, A.; Cabeza, L.F. Mainstreaming commercial CSP systems: A technology review. *Renew. Energy* **2019**, *140*, 152–176. [CrossRef]
12. Alexopoulos, S.; Hoffschmidt, B. Solar tower power plant in Germany and future perspectives of the development of the technology in Greece and Cyprus. *Renew. Energy* **2010**, *35*, 1352–1356. [CrossRef]
13. Atif, M.; Al-Sulaiman, F.A. Energy and exergy analyses of solar tower power plant driven supercritical carbon dioxide recompression cycles for six different locations. *Renew. Sustain. Energy Rev.* **2017**, *68*, 153–167. [CrossRef]
14. Awan, A.B.; Mouli, K.V.C.; Zubair, M. Performance enhancement of solar tower power plant: A multi-objective optimization approach. *Energy Convers. Manag.* **2020**, *225*, 113378. [CrossRef]
15. Habibi, H.; Zoghi, M.; Chitsaz, A.; Javaherdeh, K.; Ayazpour, M.; Bellos, E. Working fluid selection for regenerative supercritical Brayton cycle combined with bottoming ORC driven by molten salt solar power tower using energy–exergy analysis. *Sustain. Energy Technol. Assess.* **2020**, *39*, 100699. [CrossRef]
16. Boukelia, T.; Arslan, O.; Bouraoui, A. Thermodynamic performance assessment of a new solar tower-geothermal combined power plant compared to the conventional solar tower power plant. *Energy* **2021**, *232*, 121109. [CrossRef]
17. Bauer, T.; Pfleger, N.; Laing, D.; Steinmann, W.-D.; Eck, M.; Kaesche, S. High-Temperature Molten Salts for Solar Power Application. In *Molten Salts Chemistry*; Elsevier: Amsterdam, The Netherlands, 2013; pp. 415–438. [CrossRef]
18. He, Y.-L.; Cui, F.-Q.; Cheng, Z.-D.; Li, Z.-Y.; Tao, W.-Q. Numerical simulation of solar radiation transmission process for the solar tower power plant: From the heliostat field to the pressurized volumetric receiver. *Appl. Therm. Eng.* **2013**, *61*, 583–595. [CrossRef]
19. Wei, X.; Lu, Z.; Wang, Z.; Yu, W.; Zhang, H.; Yao, Z. A new method for the design of the heliostat field layout for solar tower power plant. *Renew. Energy* **2010**, *35*, 1970–1975. [CrossRef]
20. Kim, J.; Kim, J.-S.; Stein, W. Simplified heat loss model for central tower solar receiver. *Sol. Energy* **2015**, *116*, 314–322. [CrossRef]
21. Jadhav, S.; Venkatraj, V. Thermal losses in central receiver solar thermal power plant. *IOP Conf. Ser. Mater. Sci. Eng.* **2018**, *377*, 012008. [CrossRef]
22. Hasuike, H.; Yoshizawa, Y.; Suzuki, A.; Tamaura, Y. Study on design of molten salt solar receivers for beam-down solar concentrator. *Sol. Energy* **2006**, *80*, 1255–1262. [CrossRef]
23. Albarbar, A.; Arar, A. Performance Assessment and Improvement of Central Receivers Used for Solar Thermal Plants. *Energies* **2019**, *12*, 3079. [CrossRef]
24. Zhang, Q.; Wang, Z.; Du, X.; Yu, G.; Wu, H. Dynamic simulation of steam generation system in solar tower power plant. *Renew. Energy* **2019**, *135*, 866–876. [CrossRef]
25. Sorgulu, F.; Dincer, I. Design and analysis of a solar tower power plant integrated with thermal energy storage system for cogeneration. *Int. J. Energy Res.* **2019**, *43*, 6151–6160. [CrossRef]
26. Yang, H.; Li, J.; Huang, Y.; Kwan, T.H.; Cao, J.; Pei, G. Feasibility research on a hybrid solar tower system using steam and molten salt as heat transfer fluid. *Energy* **2020**, *205*, 118094. [CrossRef]
27. Chandra, L.; Dixit, A. *Concentrated Solar Thermal Energy Technologies*; Springer: Berlin/Heidelberg, Germany; New York, NY, USA, 2017.
28. Muñoz-Antón, J.; Rubbia, C.; Rovira, A.; Martínez-Val, J.M. Performance study of solar power plants with CO_2 as working fluid. A promising design window. *Energy Convers. Manag.* **2015**, *92*, 36–46. [CrossRef]
29. Liu, Y.; Wang, Y.; Huang, D. Supercritical CO_2 Brayton cycle: A state-of-the-art review. *Energy* **2019**, *189*, 115900. [CrossRef]
30. Incropera, F.P. (Ed.) *Fundamentals of Heat and Mass Transfer*, 6th ed.; John Wiley: Hoboken, NJ, USA, 2007.
31. Tsilingiris, P. Thermophysical and transport properties of humid air at temperature range between 0 and 100 °C. *Energy Convers. Manag.* **2008**, *49*, 1098–1110. [CrossRef]
32. Zaversky, F.; García-Barberena, J.; Sánchez, M.; Astrain, D. Transient molten salt two-tank thermal storage modeling for CSP performance simulations. *Sol. Energy* **2013**, *93*, 294–311. [CrossRef]

33. Alnaimat, F.; Rashid, Y. Thermal Energy Storage in Solar Power Plants: A Review of the Materials, Associated Limitations, and Proposed Solutions. *Energies* **2019**, *12*, 4164. [CrossRef]
34. Arteconi, A.; Hewitt, N.; Polonara, F. State of the art of thermal storage for demand-side management. *Appl. Energy* **2012**, *93*, 371–389. [CrossRef]
35. Wang, T. High Themal Energy Storage Density Molten Salts for Parabolic Trough Solar Power Generation. Master's Thesis, The University of Alabama, Tuscaloosa, AL, USA, 2011.
36. Chen, Y. Novel Cycles Using Carbon Dioxide as Working Fluid. Licentiate Thesis, KTH, Stocholm, Sweden, 2006.
37. Kreith, F.; Manglik, R.M.; Bohn, M.S. *Principles of Heat Transfer*, 7th ed.; Cengage Learning: Boston, MA, USA, 2011.
38. Span, R.; Wagner, W. A New Equation of State for Carbon Dioxide Covering the Fluid Region from the Triple-Point Temperature to 1100 K at Pressures up to 800 MPa. *J. Phys. Chem. Ref. Data* **1996**, *25*, 1509–1596. [CrossRef]
39. Borgnakke, C.; Sonntag, R.E. *Fundamentals of Thermodynamics*, 8th ed.; Wiley: Hoboken, NJ, USA, 2013.
40. Kaushik, S.C.; Tyagi, S.K.; Kumar, P. *Finite Time Thermodynamics of Power and Refrigeration Cycles*; Springer International Publishing: Cham, Switzerland, 2017. [CrossRef]
41. Ge, Y.; Tassou, S.; Santosa, I.D.; Tsamos, K. Design optimisation of CO_2 gas cooler/condenser in a refrigeration system. *Appl. Energy* **2015**, *160*, 973–981. [CrossRef]
42. Noone, C.J.; Torrilhon, M.; Mitsos, A. Heliostat field optimization: A new computationally efficient model and biomimetic layout. *Sol. Energy* **2012**, *86*, 792–803. [CrossRef]
43. Matweb. Aluminium 1100-H12. Available online: https://matweb.com/search/datasheet_print.aspx?matguid=e98fdee3896f4cfa8b01e232c7fe33b6 (accessed on 15 May 2023).
44. Gabbrielli, R.; Zamparelli, C. Optimal Design of a Molten Salt Thermal Storage Tank for Parabolic Trough Solar Power Plants. *J. Sol. Energy Eng.* **2009**, *131*, 041001. [CrossRef]
45. Matweb. ASTM A516 Carbon Steel, Grade 70. Available online: https://www.matweb.com/search/datasheet.aspx?matguid=9ccee2d0841a404ca504620085056e14&ckck=1 (accessed on 15 May 2023).
46. Rahman, H.; Islam, T.; Ibn Minhaj, T.; Azad, M.; Hasan, M.; Haque, A.M.R. Study of Thermal Conductivity and Mechanical Property of Insulating Firebrick Produced by Local Clay and Petroleum Coal Dust as Raw Materials. *Procedia Eng.* **2015**, *105*, 121–128. [CrossRef]
47. RSA Metal. Flexible AISI 321H Stainless Steel. Available online: https://www.rsametal.com.tr/en/stainless-steel-321h.php (accessed on 15 May 2023).
48. Mecheri, M.; Le Moullec, Y. Supercritical CO_2 Brayton cycles for coal-fired power plants. *Energy* **2016**, *103*, 758–771. [CrossRef]
49. PVGIS. Available online: https://joint-research-centre.ec.europa.eu/photovoltaic-geographical-information-system-pvgis_en (accessed on 15 May 2023).

Disclaimer/Publisher's Note: The statements, opinions and data contained in all publications are solely those of the individual author(s) and contributor(s) and not of MDPI and/or the editor(s). MDPI and/or the editor(s) disclaim responsibility for any injury to people or property resulting from any ideas, methods, instructions or products referred to in the content.